nature geoscience

Article

https://doi.org/10.1038/s41561-023-01160-z

# Submarine terraced deposits linked to periodic collapse of caldera-forming eruption columns

Received: 7 October 2022

Accepted: 27 February 2023

Johan T. Gilchrist[1], A. Mark Jellinek[1], Emilie E. E. Hooft[2] & Sean Wanket[1]

Catastrophic, caldera-forming explosive eruptions generate hazardous ash fall, pyroclastic density currents and, in some cases, tsunamis, yet their dynamics are still poorly understood. Here we use scaled analogue experiments and spectral analysis of well-preserved concentric terracing of seafloor deposits built by submarine caldera-forming explosive eruptions to provide insights into the dynamics governing these eruptions and the resultant hazards. We show that powerful submarine eruption columns in collapsing regimes deliver material to the sea surface and seabed in periodic annular sedimentation waves. Depending on the period between successive waves, which becomes shorter with decreasing jet strength, their impact and spread at the sea surface and/or seabed can excite tsunamis, drive radial pyroclastic density currents and build concentric terraces with a wavelength that decreases with distance, or deposits that thin monotonically. Whereas the Sumisu (Izu–Bonin arc) caldera deposit architecture is explained by either a subaerial or deep-water model involving no interaction between sedimentation waves and the sea surface, those of the Macauley (Kermadec arc) and Santorini (Hellenic arc) calderas are consistent with a shallow-water model with extensive sedimentation wave–sea surface–seabed interactions. Our findings enable an explicit classification of submarine caldera-forming explosive eruption dynamics and quantitative estimates of eruption rates from their terraced deposits.

Clues to the puzzling dynamics that govern mass transport and associated hazards of catastrophic caldera-forming (CCF) eruption columns[1–9] are found on the terraced slopes that appear to be an inherent feature of shallow (<1 km depth) submarine deposits surrounding calderas along volcanic island arcs, including the recently constructed deposit of the 15 January 2022 eruption of Hunga Tonga–Hunga Ha'apai[10–15] (Fig. 1a,b and Supplementary Figs. 1 and 2). Historically enigmatic, visually arresting deposits extending over tens of kilometres constructed of ~1- to 10-km-radius, ~10- to 100-m-high terraces have been linked to landslide events and resulting turbidity currents and to pyroclastic density currents (PDCs) flowing along the seafloor (submarine PDCs)[13]. Explanations of terrace field planforms, terrace widths and profile shapes, as well as the evolution and variability of these properties with distance from eruptive sources, typically rely on extensive existing studies of the steady-state dynamics of turbidity currents and PDCs, as well as marine landslides (and combinations thereof)[13,16,17]. Although insightful at individual calderas, a challenging feature of the concentric terraced deposits is that they are so common[10–15,18]: why would the dynamics of

---

[1]Department of Earth, Ocean and Atmospheric Sciences, University of British Columbia, Vancouver, British Columbia, Canada. [2]Department of Earth Sciences, University of Oregon, Eugene, OR, USA. e-mail: jgilchri@eoas.ubc.ca; mjellinek@eoas.ubc.ca; emilie@uoregon.edu; swanket@eoas.ubc.ca

gravity currents such as landslides and PDCs be expressed so similarly at calderas with disparate structures, mechanical properties, slopes and slope stabilities and with distinct volcanic source geometries and eruptive histories?

Recent analogue experiments on subaerial eruptions suggest that concentric terracing (Fig. 1c,d) is an intrinsic feature of the particle–fluid (multiphase) interactions governing the rise and descent of material in eruption columns, and spread along the ground thereafter, evolving in 'partial collapse' or 'total collapse' regimes ('collapsing regimes' hereafter)[19]. Most well-documented large CCF events in the geological record, including CCF eruptions in shallow-water environments, involve eruptive phases where half or more of the total erupted mass was delivered to PDCs[15,20–22]. In collapsing regimes that produce terraced deposits, as much as 90% of material ejected into the atmosphere is delivered back to the ground through the excitation and descent of periodic, annular sedimentation waves[19] (SWs; Fig. 1e). Critically, the minimum radius from the vent of terraces built by this mechanism is predicted to be similar to the erupting jet radius taken at its mean rise height, $H_{\mathrm{ftn}}$. While this expectation is potentially consistent with the terracing observed ~1 km adjacent to the caldera rim (in the 'near field') at Sumisu caldera (Fig. 1a), it is inconsistent with the relatively much larger radii of near-field terraces observed at Santorini (Fig. 1b) and Macauley calderas[13] (Supplementary Fig. 1). A key difference to subaerial eruption columns in collapsing regimes, however, is that the dynamics of submarine CCF events are modified by interactions with water layers, which cause the mixture to spread as it penetrates and descends[23,24]. In this article, we use analogue experiments on submarine eruptions through water layers of varying depth to show that terrace formation similarly occurs through the excitation of periodic SWs (Fig. 1c–h and Methods) and that this process is probably a generic feature of CCF events. We show that this process and its expression in the architectures of resulting deposits are highly sensitive to, and diagnostic of, both eruptive source and water depth conditions. We also show that the structural characteristics of terraces closest to the caldera rim record the effects of erosion and sedimentation related to the impact and spread of SWs at the seabed as PDCs, consistent with earlier studies[13]. Taken together, our results strengthen an emerging framework for classifying eruption column collapse deposits, quantitatively constraining eruption source parameters from qualitative observations of deposit architectures and understanding the timing and intensity of tsunami and PDC hazards related to CCF eruptions[19,25].

## Periodic sedimentation waves build terraces

CCF events at the Santorini, Sumisu, and Macauley (Supplementary Information) calderas[13] each delivered mixtures of ash, gases and water vapour to the atmosphere through a shallow water layer. Each also produced deposits marked by sharply defined, approximately concentric and periodic terraces with low-slope, backward-facing profiles (Figs. 1a,b and 2a,b and Supplementary Fig. 1). Terraces at Santorini and Macauley decline monotonically in wavelength from order 1,000 to 100 m over 10–16 km radial profiles. This pattern of wavelength decline is also evident in profiles from the northeastern terraces around Sumisu[11] (Figs. 1a and 2b). However, significant differences in the deposit architectures occur. Whereas terraces are approximately planar ~1 km from the caldera rim in the near field at Sumisu, near-field terraces with concave backward profiles at Santorini and Macauley calderas occur ~3–6 km from the caldera rim (Figs. 1a,b and 2a,b and Supplementary Fig. 1). Furthermore, there is a relatively wide and deep trough between the rim of Macauley caldera and the start of the near-field terraces that is not present at Santorini or Sumisu (Supplementary Fig. 1).

To investigate links among eruption column collapse dynamics, SWs and the construction of terraced deposits during CCF events in submarine settings, we conduct carefully scaled analogue experiments on turbulent particle–water fountains injected into water layers of varying depths and analyse the fountain-top height oscillations and geometry of their deposits (Methods, Figs. 1e,f, 2e,f and 3a,b, Supplementary Fig. 2, Supplementary Table 1 and Supplementary Videos 1–4). In this article, we focus on the dynamics governing the delivery of dense mixtures of coarse pyroclastic material in SWs to the water surface (free surface) and seafloor, which forms the major volume of the erupted material[15,20–22]. Our experiments do not model the delivery of fine ash to the upper troposphere and stratosphere by buoyant plumes of interstitial gas that escape the collapsing part of the eruption column where it stalls at or near the maximum 'fountain height', ~$H_{\mathrm{ftn}}$ (refs. 26,27). We also neglect complex effects of transient, spatially varying layers of floating pumice (pumice rafts) on SW-free-surface interactions[28] (further discussion in Methods).

In 'deep-water' experiments, the water-layer depth $h_{\mathrm{w}} \gg H_{\mathrm{ftn}}$ (equation (5); Figs. 1e and 3a), whereas in shallow-water experiments $h_{\mathrm{w}} \leq H_{\mathrm{ftn}}$ (Figs. 1f and 3b and Supplementary Videos 1 and 2). Our previous work shows that in collapsing regimes in air or deep water, eruption columns collapse periodically as annular SWs to deliver material to an impact zone (Figs. 1e,g and 3a; fig. 20 in ref. 19). The excitation of SWs is driven by the periodic accumulation and release of dense material at $H_{\mathrm{ftn}}$, which excites oscillations of the fountain top at distinct fountain and environmental stratification frequencies[29] (equations (6) and (7), respectively). Usefully, the fountain frequency predicts the timing between SWs and resulting PDCs, which govern the architecture of the terraced deposits (Methods and Fig. 3a; fig. 17 in ref. 19).

For shallow-water experiment #11, four distinct oscillation periods are identified in the subaerial fountain-top height time series (Fig. 3c,d and Supplementary Fig. 2) and agree with predicted $1/f_{\mathrm{ftn}}$, $1/N_{\mathrm{wtr}}$ and $1/N_{\mathrm{air}}$ from source and environmental conditions, as well as $1/f_{\mathrm{e}}^{\mathrm{sw}}$ measured by tracking SW descent speed and radius. Overall, we find that shallow-water fountains input energy to the stratification at $f_{\mathrm{ftn}}^{\mathrm{wtr}}$ and excite the higher frequencies $N_{\mathrm{wtr}}$, $N_{\mathrm{air}}$, $f_{\mathrm{ftn}}^{\mathrm{air}}$ and $f_{\mathrm{e}}^{\mathrm{sw}}$. Energy is dissipated at frequencies above $f_{\mathrm{e}}^{\mathrm{sw}}$ predominantly through molecular mixing across the air–water density interface[30].

In the absence of a water layer or under deep-water conditions, SWs carry a momentum flux that increases in proportion to $H_{\mathrm{ftn}}$. Depending on $H_{\mathrm{ftn}}$ and the extent to which entrainment and mixing reduce the density excess driving the descent of these mixtures, SWs can either impact the ground or seabed as jets that drive intense scouring and erosion or become largely dissipated descending clouds of dense particles. Deposition from such relatively quiescent particle clouds is mostly by individual particle settling[19,31]. By contrast, where strong impacts occur, SWs evolve into axisymmetric PDCs that deposit regularly spaced and axisymmetric terraces (Figs. 1c,e,g and 2e,f). Geometrically, terraces are confined within a characteristic impact zone with radius $r_{\mathrm{im}}$ from the jet margin that is comparable to the jet diameter.

Under shallow-water conditions, SWs descending through air impact the free surface and excite water waves (analogue tsunamis) (Fig. 1f,h and Supplementary Videos 1 and 2). The momentum-driven spread of the mixture and its overshoot across the free surface as an erosive jet can scour the seabed, depending on the water-layer height $h_{\mathrm{w}}$. A useful metric to characterize SW interactions with the seabed is, thus, the dimensionless penetration depth

$$D_{\mathrm{sw}} = \frac{H}{l_{\mathrm{sw}}}, \qquad (1)$$

where $H = H_{\mathrm{ftn}}$ for subaerial or deep-water conditions or $H = h_{\mathrm{w}}$ for shallow-water conditions and $l_{\mathrm{sw}}$ is a characteristic scale for the overshoot depth of an SW (equation (9)), which can also be inferred observationally. If $D_{\mathrm{sw}} > 1$, pyroclastic particle settling within the impact zone will form a nearly planar terrace. By contrast, if $D_{\mathrm{sw}} \leq 1$, descending SWs impact and spread at the seabed within the impact zone as erosive jets that deposit backward-facing terraces. In the special limit $D_{\mathrm{sw}} \ll 1$, intensive scouring produces a distinctive concave backward-facing terrace architecture (Fig. 4). In this case, $D_{\mathrm{sw}}$ predicts also a 'scouring

https://doi.org/10.1038/s41561-023-01160-z

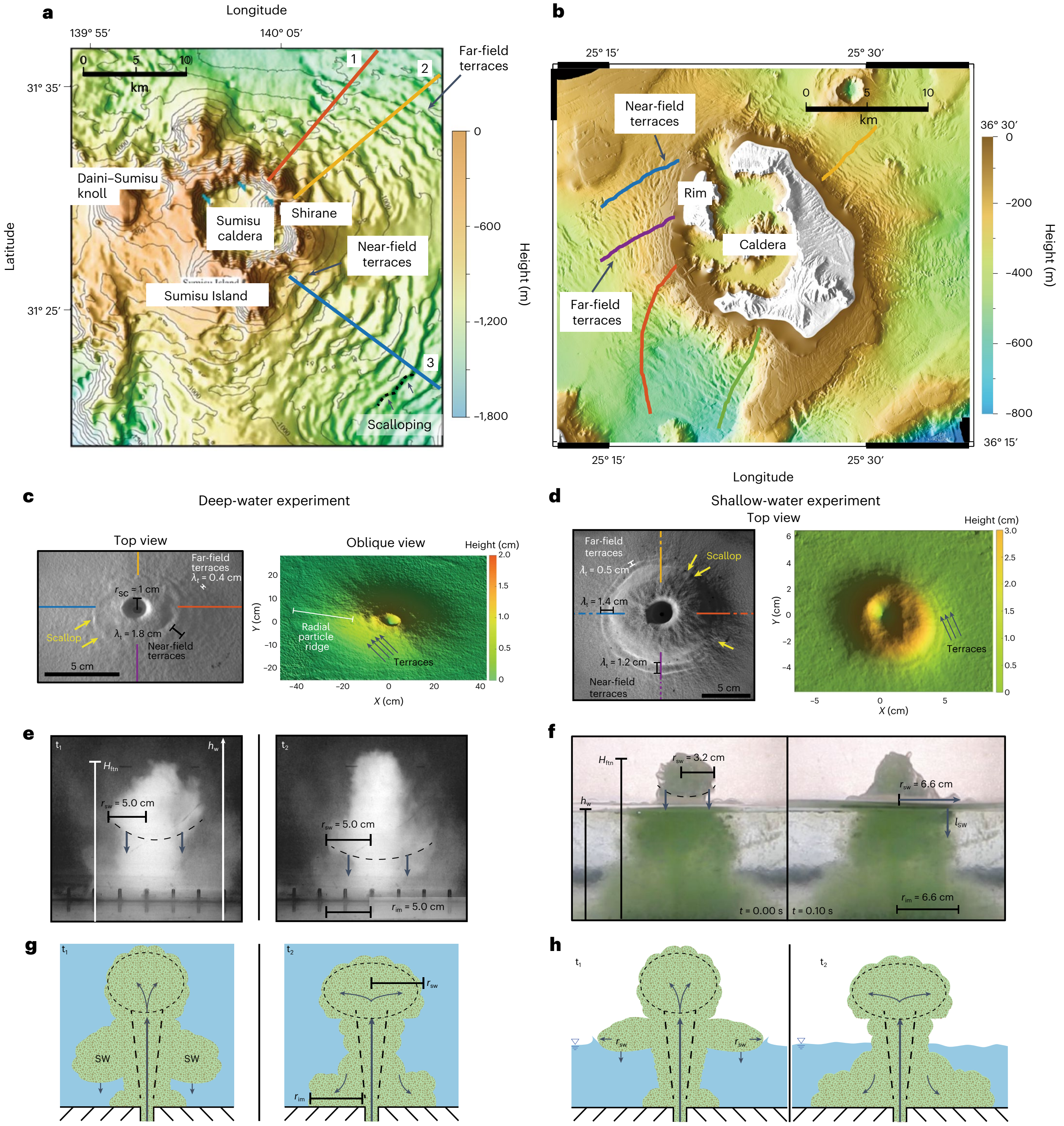

**Fig. 1 | Terraced deposits surrounding calderas and analogue experiments.** **a**, Sumisu caldera (Izu–Bonin arc) bathymetry showing terracing of the shallow submarine pyroclastic deposit (30–60 thousand years ago)[11]. **b**, Bathymetry of the shallow submarine terraced pyroclastic deposit surrounding Santorini caldera (Greece, 3.6 thousand years ago[10,14]). Positive and negative latitude values correspond to North and South of the equator, respectively. Similarly, positive and negative longitude values correspond to East and West of the prime meridian, respectively. **c**, Left image shows terraced deposit built by deep-water experiment #10 (Supplementary Table 1) with marked scouring radius $r_{sc}$ and terrace wavelengths ($\lambda$). Right figure shows a vertically exaggerated digital elevation model of deposits, where radial particle ridges are marked by white line. **d**, Shallow-water experiment #6 deposit marked similarly as in **c**. **e**,**f**, Image pairs of a descending SW in deep-water experiment #32 (**e**) and shallow-water experiment #6 (**f**) where $r_{sw}$ is the SW radius, $l_{sw}$ is the SW jet entrance length into the water layer (equation (9)) and $t$ is time. **g**,**h**, Conceptual model cartoons of a descending SW in a deep-water (**g**) and a shallow-water (**h**) experiment. Panel **a** reproduced with permission from ref. 11, Springer Nature Limited.

radius' $R_{sc} = r_{sc}/r_0$, where $r_{sc}$ is the radius of the scoured region of the deposit and $r_0$ is the vent radius (Fig. 1c). Of practical value (SWs and shallow water layers in collision), field measurements of the scouring radius can constrain the water depth and momentum flux carried by SWs. Furthermore, if the frequency at which SWs impact the free surface is higher than the frequency at which spreading SWs descend to

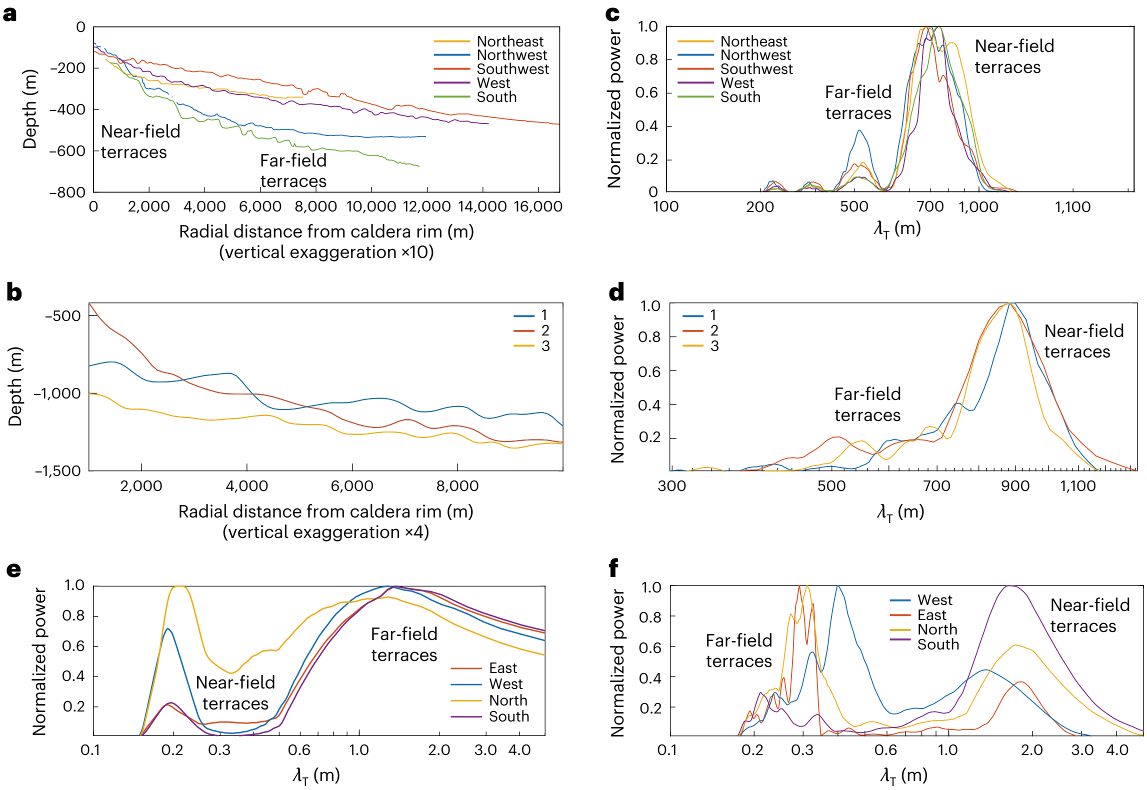

**Fig. 2 | Radial profiles and power spectra of terraced deposits. a**,**b**, Radial deposit profiles showing backward-facing terraces with low-slope, planar upper surfaces around Santorini (**a**) and Sumisu (**b**) calderas. Relatively high slopes down gradient from sharp terrace crests are common characteristics of terrace morphometry. Profiles are colour coded to their locations in Fig. 1a,b. **c**,**d**, Normalized power spectra of deposit profiles from Santorini (**c**) and Sumisu (**d**) shown in Fig. 1 estimated with a standard Thompson multitaper algorithm. Spectral results of deposit profiles shown in Fig. 1a,b show a remarkable radial symmetry with power concentrated in the larger near-field terraces and a fall off with distance that is relatively smooth at Sumisu. **e**,**f**, Power spectra of deposit topography profiles shown in Fig. 1c,d for shallow-water experiment (**e**) and deep-water experiment (**f**) with near- and far-field terrace wavelength peaks marked.

the seabed, interactions between successive SWs spreading at the free surface can augment the delivery of erupted mass and momentum flux to growing deposits (Figs. 3b and 5 and Supplementary Video 1).

## SWs and shallow water layers in collision

A number of key geometric properties of terraces observed around Sumisu, Santorini and Macauley calderas place restrictive constraints on the mechanics of their formation. In plan view, broad, regular concentric terraces with scalloped edges have a wavelength that declines with distance from caldera rims (Figs. 1a,b and 2a–e and Supplementary Figs. 1 and 3). In profile, terraces are sharply defined and backward facing with planar (Sumisu) or concave (Macauley and Santorini) (Fig. 2a,b and Supplementary Fig. 1) upper surfaces that are most apparent in the near field. Seismic reflection profiles at Macauley show (eruption-derived) ‘ponded volcaniclastic sediments’ within an ~3-km-wide concave region[13] (Supplementary Fig. 1). Furthermore, the occurrence of intermittent tsunamis is often associated with historic shallow-water caldera eruptions[32–34], suggesting an intermittent tsunamigenic process during eruptions.

Our analogue terraced deposits are diagnostic of eruption intensity in collapsing regimes and have planforms and radial profiles that are sensitive to the water-layer and SW penetration depths $D_{sw}$. Consistent generally with deposits at Sumisu, Santorini and Macauley calderas, analogue deposits are constructed of regularly spaced, concentric and backward-facing terraces with broad, low-slope top surfaces, sharp crests and relatively short, high-slope downstream sides. Evident visually (Figs. 1c,d, 4 and 5) and spectrally (Fig. 2e,f), periodic terrace widths also decline with radial distance from the near to far field of experimental deposits. Akin to deep-water experiments under intermediate or strong eruptive conditions, the backward-facing Sumisu deposit terraces are also characterized by azimuthal scalloping along terrace edges over scales smaller than terrace widths in the near field and comparable to the terrace widths in the far field. By contrast, concavity in near-field Santorini and particularly Macauley terraces signal both $h_w \ll H_{ftn}$ and $D_{sw} < 1$ conditions and require that these events be very strong eruptions (Figs. 1b, 2a and 5). Indeed, the ~2-km-wide concavity containing eruption-derived material at Macauley is consistent with intense excavation within an impact zone under potentially extreme $D_{sw} \ll 1$ conditions.

Quantitatively, water depth and eruption fountain strength are indicated from the deposit architecture through a Richardson number–particle volume fraction ($-\mathrm{Ri}_0 \leftrightarrow \phi_0$) regime diagram derived from our experiments (Fig. 5 and equations (2) and (3) in Methods). In deep-water regimes, the number and maximum radii of terraces decrease as fountains become weaker or more concentrated. In shallow-water cases, the water depth exerts the primary control over the extent to which SWs scour or deposit sediment in the near-field deposit (Fig. 4). Lateral scouring and concavity are intensified as $D_{sw} \to 0$, whereas near-field terraces become increasingly planar as $D_{sw}$ approaches and exceeds 1. Deposit architecture can be combined with plausible estimates of eruption source parameters to constrain the fountain strength, particle volume fraction and mass eruption rate (MER) of CCF eruptions (Fig. 5 and Methods). MER exerts a profound control over eruptive behaviour and is the greatest source of uncertainty in computational models of

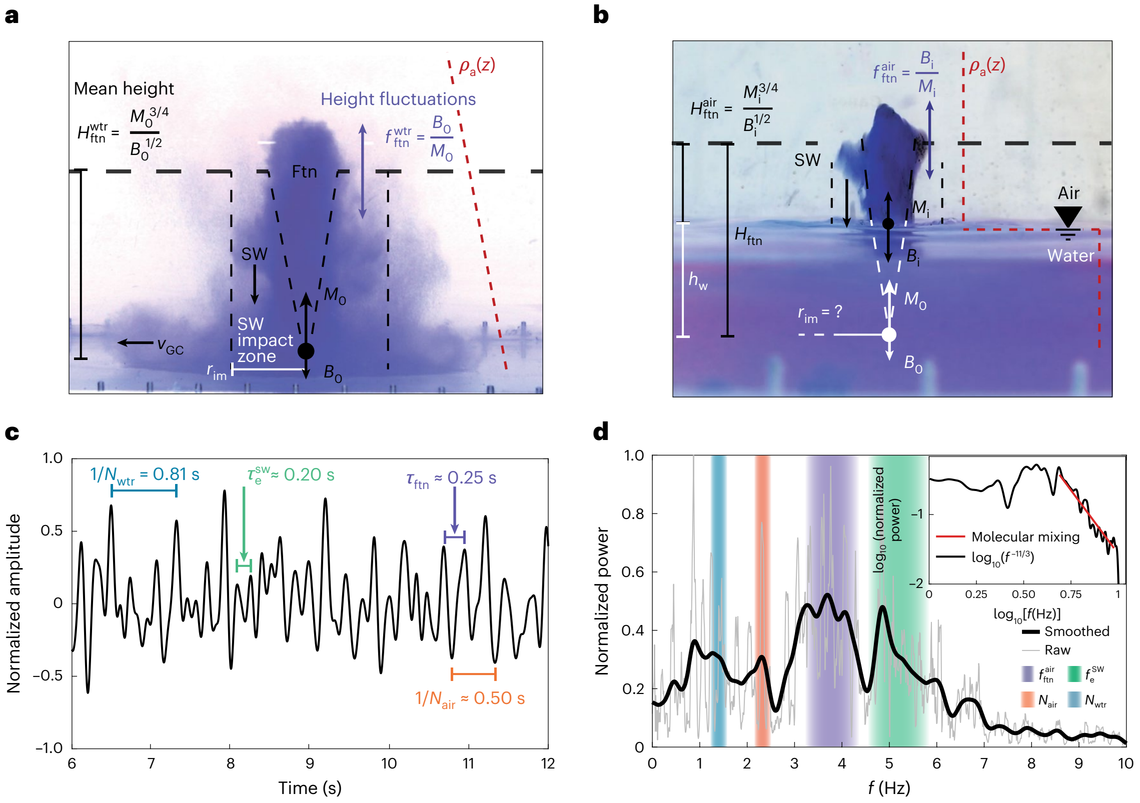

**Fig. 3 | Fountain-top height oscillations linked to water depth and SW dynamics. a**, Image of a coarse particle–saltwater fountain (purple) rising in a density-stratified ($\rho_a(z)$) saltwater ambient (transparent) during a deep-water experiment. Ftn, fountain; SW, descending SW; $M_0$, source momentum flux; $B_0$, source buoyancy flux; $M_i$, interfacial momentum flux, $B_i$, interfacial buoyancy flux; $r_{im}$, radius of the SW impact zone; $v_{GC}$, the ground-hugging gravity current spreading speed. **b**, Image of a coarse particle fountain breaching the air–water interface midway through a shallow-water experiment. **c**, Steady-state section of shallow-water fountain-top height time series (dotted box in Supplementary Fig. 3) where the SW overturn $\tau_e^{sw} = 1/f_e^{sw}$, fountain collapse $\tau_{ftn} = 1/f_{ftn}^{air}$ and stratification oscillation periods, for the fountain rise through the water $1/N_{wtr}$ and air columns $1/N_{air}$, are identified. **d**, Power spectrum of fountain-top height fluctuations where characteristic frequencies ($f$) are marked with separate colours within uncertainties. Inset graph shows power spectrum in log–log space with power law (red) indicating energy dissipation through irreversible mixing across density interfaces[19,30].

eruptions aimed at understanding PDC hazards as well as volcanic effects on climate[24,35,36]. To our knowledge this is the first attempt at a reconstruction of CCF eruption source parameters from deposit architectures.

## Generic model for terrace formation by SWs

We combine experimental results related to the periodic delivery of material in SWs with established models of flow and sedimentation by PDCs and turbidity currents to construct a generic conceptual model for the formation and evolution of terraced deposits related to successive SWs[19,37–39] (Fig. 6). During a shallow-water eruption, an initial SW impacts the free surface and spreads, generating interfacial waves (analogue tsunamis) (Fig. 6a). If $D_{sw} \ll 1$, the SW impacts and scours the seabed over a distance $r_{sc}$ (Fig. 4), deposits material to form a terrace (Fig. 1) and drives a ground-hugging gravity current (Fig. 6a–d). Subsequent SWs impact and further scour the first terrace before they spread and deposit material downstream (Fig. 6e). Successive flows are modulated by interactions with evolving deposit topography through the production and draining of standing waves formed at hydraulic jumps at the downstream edges of terraces (Fig. 6e). A similar overall evolution occurs in deep-water experiments where $D_{sw} \leq 1$, albeit with less scouring of the deposit by successive SWs (deep-water experiments in Figs. 5 and 6g). It is important to note that this model applies only to deposition on relatively shallow and smooth slopes that are below the angle of repose of the particle size distribution carried by PDCs.

The primary effect of a shallow water layer on this terrace formation process is to cause SWs to stall and spread as they overshoot the free surface before their descent and impact with the seabed. This process introduces an important additional link between deposit architecture and the eruption dynamics through a 'collapse frequency' number $\mathcal{F}_C$ (equation (10)). Key to the evolution summarized in Fig. 6 is the time between successive SWs. If $\mathcal{F}_C \gg 1$, SWs collapse in quick succession to combine or otherwise interact strongly before descending to the seabed or at the seabed, periodic terracing is inhibited and eruptions produce massive deposits, which is observed for the weakest events in our experimental results (Fig. 5). By contrast, as $\mathcal{F}_C \rightarrow 0$, the period between column collapses is long enough that PDCs can flow out of the SW impact zone $r_{im}$ as discrete events to build terraces in the near-field deposit with distinct bedding. In this case, however, if $D_{sw} \rightarrow 0$, deposit terraces adjacent to the caldera rim will be scoured (Figs. 4 and 5). Taken together, $\mathcal{F}_C$ and $D_{sw}$ provide explicit links among eruption source parameters, column dynamics, SWs, PDCs and deposit architecture.

Quantitatively, our results suggest that strong eruption columns in collapsing regimes will drive periodic rather than continuous PDCs to make terraced deposits where $-\mathrm{Ri}_0 \gtrsim 10^{-4}$ and $\mathcal{F}_C < 1$ (Fig. 5). Such dynamics involving intense SW–water surface interactions will lead also to tsunamis[32] and potentially to a greater likelihood for over-water and amphibious PDCs[40]. More generally, the inherent control of $\mathcal{F}_C$ over deposit architecture is not restricted to submarine events. Akin to the deep-water experiments, low-strength CCF eruption columns on land will also have a greater proclivity to produce massive deposits, consistent with previous studies[25,41,42]. Whether subaerial terraced deposits

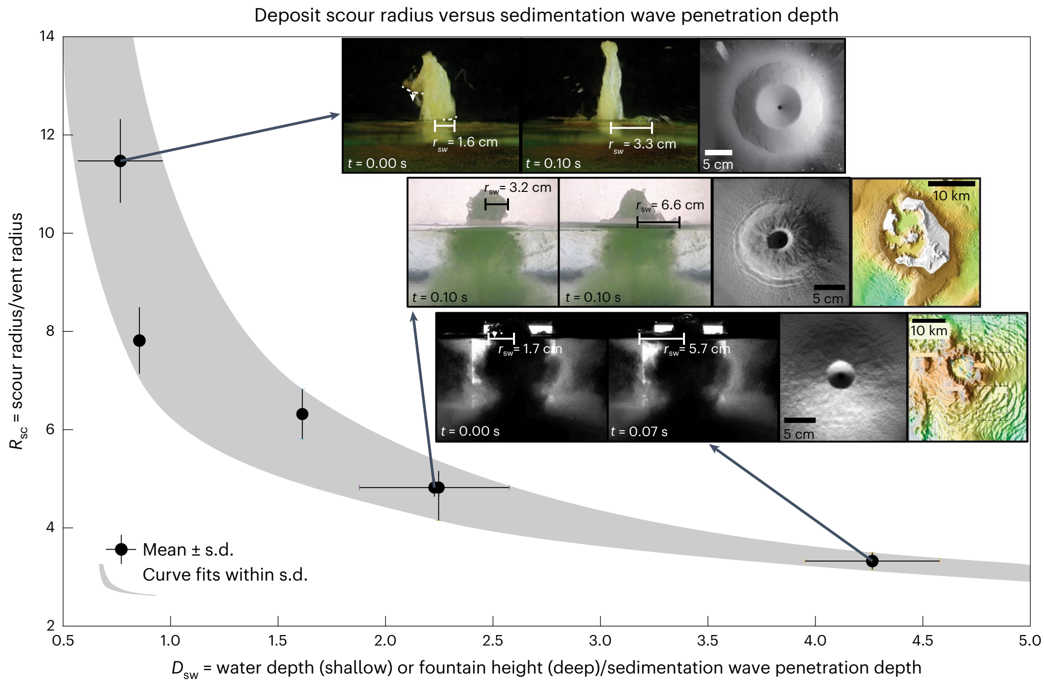

**Fig. 4 | Deposit scour radius as a function of SW penetration depth.** Scouring radius $R_{sc}$ of deposit as a function of SW penetration depth $D_{sw}$. The first two insets in each row of images show an SW descending around the subaerial region of a shallow-water fountain and then impacting the air–water interface, with $r_{sw}$ marked. The third insets are top-view images of the resulting deposit. Fourth insets in the middle and bottom panels show the terraced deposits of Santorini and Sumisu, respectively.

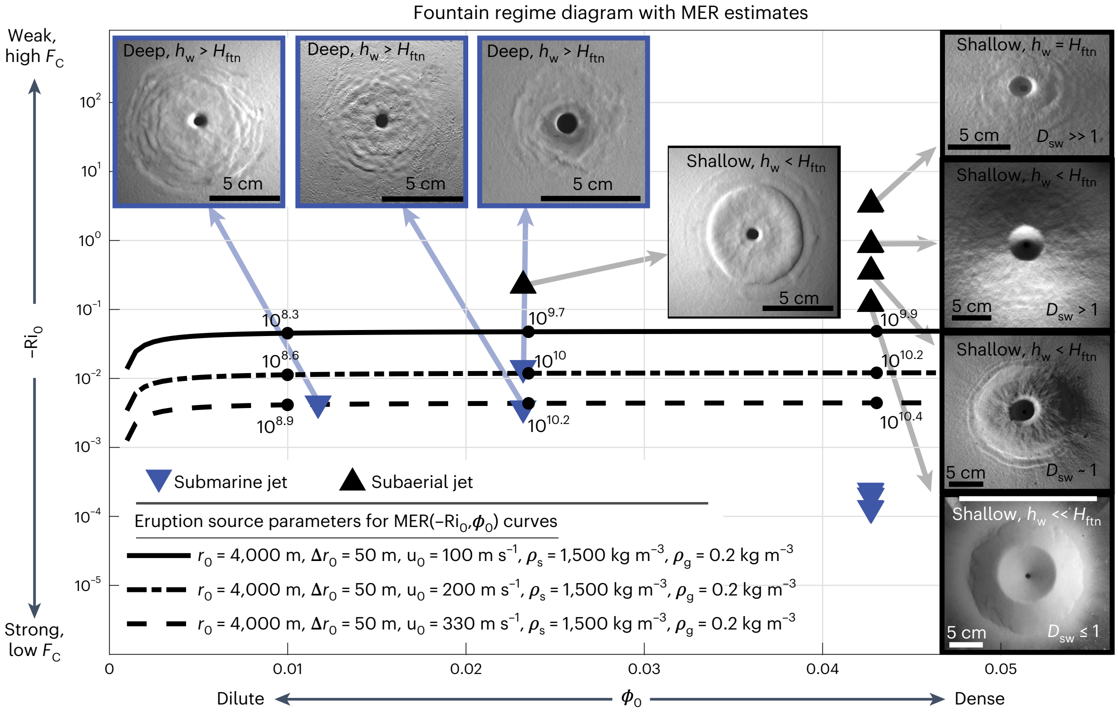

**Fig. 5 | Fountain strength versus particle volume fraction regime diagram.** Deep- and shallow-water fountain experiments plotted in a source Richardson number–particle volume fraction parameter space (Methods). As the magnitude of the source Richardson number $-Ri_0$ decreases, the 'strength' of the eruption increases and the SW collapse frequency $\mathcal{F}_C$ declines. For deep-water eruptions, $-Ri_0$ is defined on the basis of submerged vent conditions (filled blue triangles). In very shallow-water regimes where $D_{sw} \ll 1$, most of the eruption column is above the free surface, and it is more appropriate to define eruption strength in terms of properties in air or $-Ri_{air}$ (filled black triangles). Where $h_w \leq H_{ftn}$, both definitions can be useful. Solid, dashed and dash-dot MER curves are calculated for inferred plausible caldera-ring vent source parameters[21,35] (Methods). Reconstructed eruption rates for $D_{sw} \leq 1$ are consistent with expectations on the basis of recent calculations by ref. 24, which conservatively limit water depths to be 100–200 m.

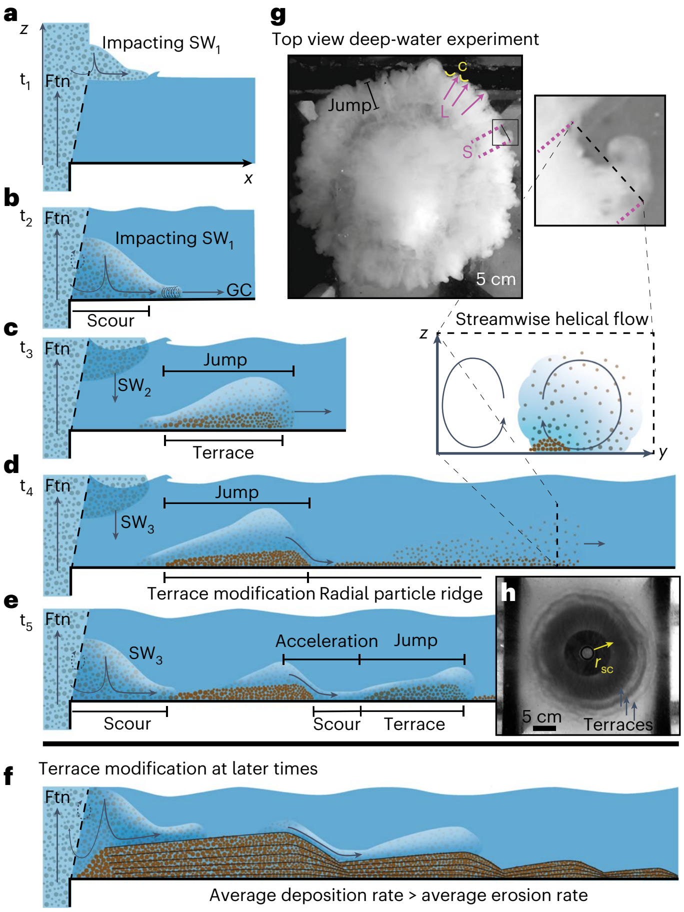

**Fig. 6 | Terrace formation by SWs. a–e**, Conceptual model cartoons of terraced and radial particle ridge deposit formation. Ground-hugging gravity currents shown in blue graded to light blue colours with particles shown in brown. The first three SWs are marked as $SW_1$, $SW_2$ and $SW_3$. **f**, Terrace modification by SWs and ground-hugging gravity currents at later times. **g**, SWs spreading as ground-hugging gravity currents developing groovy instabilities[39] during a deep-water experiment with only fine particles (further discussion in Supplementary Information). A surging ground-hugging gravity current is marked 'S', with lobe 'L' and cleft 'C' structures of other surging currents marked. Cross-section cartoon of streamwise helical flow corresponds to black boxes in **d** and **g**. Top view of an annular nozzle deposit from our previous work[22] showing scoured regions between terraces of decreasing wavelength with radial distance.

exist to test this link is currently unknown as terraces can be buried by pyroclastic material erupted later or after a CCF event (Supplementary Fig. 3). Building on our previous study[19], here we constrain minimum $-\mathrm{Ri}_0 - \phi_0$ values where terracing is expected to occur for subaerial and submarine eruption columns in collapsing regimes. Future studies should investigate the maximum $-\mathrm{Ri}_0 - \phi_0$ eruption column parameter space where $\mathcal{F}_C$ transitions from supplying discrete to continuous mass fluxes to spreading PDCs and whether this is expressed as a transition in near-field deposits from bedded and terraced architectures to massive architectures absent of terraces.

Our experimental results show that qualitative observations of terraced deposit architectures related to CCF events are linked to underlying eruption column dynamics and can quantitatively constrain source parameters of eruption columns in collapsing regimes. The potential to use these data to bound MERs, which are critical inputs for models and historically challenging to infer from observations[36], provides exciting ways to study both submarine and subaerial eruption deposits. More broadly, understanding how the dynamics of PDCs driven by periodic SWs are potentially modified by evolving particle–fluid coupling regimes will also have implications for the flow of turbidity currents along the seafloor and rock and snow avalanches on land[43].

## Online content

Any methods, additional references, Nature Portfolio reporting summaries, source data, extended data, supplementary information, acknowledgements, peer review information; details of author contributions and competing interests; and statements of data and code availability are available at https://doi.org/10.1038/s41561-023-01160-z.

## References

1. Rampino, M. R. & Self, S. Volcanic winter and accelerated glaciation following the Toba super-eruption. *Nature* **359**, 50–52 (1992).
2. Robock, A. et al. Did the Toba volcanic eruption of ~74 ka BP produce widespread glaciation? *J. Geophys. Res. Atmos*. https://doi.org/10.1029/2008JD011652 (2009).
3. Williams, M. The 73 ka Toba super-eruption and its impact: history of a debate. *Quat. Int*. **258**, 19–29 (2012).
4. Raible, C. C. et al. Tambora 1815 as a test case for high impact volcanic eruptions: Earth system effects. *Wiley Interdiscip. Rev. Clim.Change* **7**, 569–589 (2016).
5. Driessen, J. The Santorini eruption. an archaeological investigation of its distal impacts on minoan crete. *Quat. Int*. **499**, 195–204 (2019).
6. Druitt, T. H., McCoy, F. W. & Vougioukalakis, G. E. The late Bronze Age eruption of Santorini volcano and its impact on the ancient Mediterranean world. *Elements* **15**, 185–190 (2019).
7. Black, B. A., Lamarque, J.-F., Marsh, D. R., Schmidt, A. & Bardeen, C. G. Global climate disruption and regional climate shelters after the Toba supereruption. *Proc. Natl Acad. Sci. USA* **118**, e2013046118 (2021).
8. Lespez, L. et al. Discovery of a tsunami deposit from the Bronze Age Santorini eruption at Malia (Crete): impact, chronology, extension. *Sci. Rep*. **11**, 15487 (2021).
9. Schmidt, A. & Black, B. A. Reckoning with the rocky relationship between eruption size and climate response: toward a volcano–climate index. *Annu. Rev. Earth Planet. Sci*. **50**, 627–661 (2022).
10. Sigurdsson, H. et al. Marine investigations of Greece's Santorini volcanic field. *Eos* **87**, 337–342 (2006).
11. Tani, K. et al. Sumisu volcano, Izu–Bonin arc, Japan: site of a silicic caldera-forming eruption from a small open-ocean island. *Bull. Volcanol*. **70**, 547–562 (2008).
12. Rotella, M. D., Wilson, C. J., Barker, S. J. & Wright, I. C. Highly vesicular pumice generated by buoyant detachment of magma in subaqueous volcanism. *Nat. Geosci*. **6**, 129–132 (2013).
13. Pope, E. L. et al. Origin of spectacular fields of submarine sediment waves around volcanic islands. *Earth Planet. Sci. Lett*. **493**, 12–24 (2018).
14. Hooft, E. E. et al. Backarc tectonism, volcanism, and mass wasting shape seafloor morphology in the Santorini–Christiana–Amorgos region of the Hellenic volcanic arc. *Tectonophysics* **712**, 396–414 (2017).
15. Seabrook, S. et al. Pyroclastic density currents explain far-reaching and diverse seafloor impacts of the 2022 Hunga Tonga Hunga Ha'apai eruption. Preprint at *Research Square* https://doi.org/10.21203/rs.3.rs-2395332/v1 (2023).
16. Wynn, R. B., Weaver, P. P., Ercilla, G., Stow, D. A. & Masson, D. G. Sedimentary processes in the selvage sediment-wave field, NE Atlantic: new insights into the formation of sediment waves by turbidity currents. *Sedimentology* **47**, 1181–1197 (2000).
17. Lee, H. J. et al. Distinguishing sediment waves from slope failure deposits: field examples, including the 'Humboldt slide', and modelling results. *Mar. Geol*. **192**, 79–104 (2002).

18. Wright, I., Worthington, T. & Gamble, J. New multibeam mapping and geochemistry of the 30–35° S sector, and overview, of southern Kermadec arc volcanism. *J. Volcanol. Geothermal Res.* **149**, 263–296 (2006).
19. Gilchrist, J. T. & Jellinek, A. M. Sediment waves and the gravitational stability of volcanic jets. *Bull. Volcanol.* **83**, 64 (2021).
20. Kaminski, É. & Jaupart, C. Marginal stability of atmospheric eruption columns and pyroclastic flow generation. *J. Geophys. Res.* **106**, 21785 (2001).
21. Carazzo, G., Kaminski, E. & Tait, S. On the dynamics of volcanic columns: a comparison of field data with a new model of negatively buoyant jets. *J. Volcanol. Geothermal Res.* **178**, 94–103 (2008).
22. Jessop, D., Gilchrist, J., Jellinek, A. & Roche, O. Are eruptions from linear fissures and caldera ring dykes more likely to produce pyroclastic flows? *Earth Planet. Sci. Lett.* **454**, 142–153 (2016).
23. Cahalan, R. & Dufek, J. Explosive submarine eruptions: the role of condensable gas jets in underwater eruptions. *J. Geophys. Res. Solid Earth* **126**, e2020JB020969 (2021).
24. Rowell, C. R., Jellinek, A. M., Hajimirza, S. & Aubry, T. J. External surface water influence on explosive eruption dynamics, with implications for stratospheric sulfur delivery and volcano–climate feedback. *Front. Earth Sci.* https://doi.org/10.3389/feart.2022.788294 (2022).
25. Giordano, G. & Cas, R. A. Classification of ignimbrites and their eruptions. *Earth Sci. Rev.* **220**, 103697 (2021).
26. Cas, R. A. & Simmons, J. M. Why deep-water eruptions are so different from subaerial eruptions. *Front. Earth Sci.* **6**, 198 (2018).
27. Maeno, F. et al. Seawater–magma interactions sustained the high column during the 2021 phreatomagmatic eruption of Fukutoku-Oka-no-Ba. *Commun. Earth Environ.* **3**, 260 (2022).
28. Fauria, K. E. & Manga, M. Pyroclast cooling and saturation in water. *J. Volcanol. Geothermal Res.* **362**, 17–31 (2018).
29. Burridge, H. & Hunt, G. The rhythm of fountains: the length and time scales of rise height fluctuations at low and high froude numbers. *J. Fluid Mech.* **728**, 91–119 (2013).
30. Ozmidov, R. V. On the turbulent exchange in a stably stratified ocean. *Atmos. Ocean. Phys.* **1**, 853–860 (1965).
31. Bush, J. W., Thurber, B. & Blanchette, F. Particle clouds in homogeneous and stratified environments. *J. Fluid Mech.* **489**, 29–54 (2003).
32. Self, S. & Rampino, M. R. The 1883 eruption of Krakatau. *Nature* **294**, 699–704 (1981).
33. Sigurdsson, H., Carey, S., Mandeville, C. & Bronto, S. Pyroclastic flows of the 1883 Krakatau eruption. *Eos* **72**, 377–381 (1991).
34. Terry, J. P., Goff, J., Winspear, N., Bongolan, V. P. & Fisher, S. Tonga volcanic eruption and tsunami, January 2022: globally the most significant opportunity to observe an explosive and tsunamigenic submarine eruption since AD 1883 Krakatau. *Geosci. Lett.* **9**, 24 (2022).
35. Costa, A., J Suzuki, Y. & Koyaguchi, T. Understanding the plume dynamics of explosive super-eruptions. *Nat. Commun.* **9**, 654 (2018).
36. Aubry, T. J. et al. The independent volcanic eruption source parameter archive (IVESPA, version 1.0): a new observational database to support explosive eruptive column model validation and development. *J. Volcanol. Geothermal Res.* **417**, 107295 (2021).
37. Hall, B., Meiburg, E. & Kneller, B. Channel formation by turbidity currents: Navier–Stokes-based linear stability analysis. *J. Fluid Mech.* **615**, 185–210 (2008).
38. Cartigny, M. J., Ventra, D., Postma, G. & van Den Berg, J. H. Morphodynamics and sedimentary structures of bedforms under supercritical-flow conditions: new insights from flume experiments. *Sedimentology* **61**, 712–748 (2014).
39. Kieffer, S. W., Meiburg, E., Best, J. & Austin, J. The mysterious grooves of Volcán Bárcena: a review of the role of streamwise counter-rotating vortices during erosion by dilute pyroclastic density currents. *Bull. Volcanol.* **83**, 26 (2021).
40. Dufek, J. & Bergantz, G. W. Dynamics and deposits generated by the Kos Plateau Tuff eruption: controls of basal particle loss on pyroclastic flow transport. *Geochem. Geophys. Geosysyt.* https://doi.org/10.1029/2007GC001741 (2007).
41. Rowley, P. D., Macleod, N. S., Kuntz, M. A. & Kaplan, A. M. Proximal bedded deposits related to pyroclastic flows of May 18, 1980, Mount St. Helens, Washington. *Geol. Soc. Am. Bull.* **90**, 2929–2947 (1985).
42. Roche, O., Buesch, D. C. & Valentine, G. A. Slow-moving and far-travelled dense pyroclastic flows during the Peach Spring super-eruption. *Nat. Commun.* **7**, 10890 (2016).
43. Lube, G., Breard, E. C., Esposti-Ongaro, T., Dufek, J. & Brand, B. Multiphase flow behaviour and hazard prediction of pyroclastic density currents. *Nat. Rev. Earth Environ.* **1**, 348–365 (2020).

## Methods

Here we describe our experimental method and scaling parameters that characterize eruptive and experimental source parameters[44]. We then show how the periodic properties of deposit terrace profiles are analysed to identify near- and far-field terrace wavelengths.

To model submarine explosive eruptions, we inject turbulent mixtures of water and silica particles with a constant flow rate into water layers deeper or shallower than the jet-rise height (deep-water and shallow-water experiments, respectively; Figs. 1e,f and 3a,b). For deep-water experiments, flows are injected into a density-stratified salt-water layer whereas for shallow-water experiments, they are injected into a constant-density water layer. We use 'fine' $d_\mathrm{p} = 75 \pm 25$ µm and 'coarse' $d_\mathrm{p} = 225 \pm 25$ µm diameter particles with densities of $\rho_\mathrm{f} = 2{,}525$ kg m$^{-3}$ and $\rho_\mathrm{c} = 2{,}693$ kg m$^{-3}$, respectively, that simulate the inertial effects of fine and coarse ash on volcanic jet dynamics[22,45]. Applying experimental methodologies detailed in ref. 19, we characterize analogue eruption column behaviour quantitatively with a combination of high-resolution colour and greyscale images captured at 30 fps and 124 fps, respectively. Digital elevation models of analogue terraced deposits are produced after carefully draining experimental tanks with structure-from-motion photogrammetry carried out with Agisoft Metashape software.

The rise of both analogue and natural jets requires entrainment (and turbulent mixing). For entrainment to occur, work is extracted from the velocity field imparted at the mixture source to penetrate, overturn and engulf less-dense ambient fluid or atmosphere. The underlying balance between stabilizing buoyancy and driving inertial forces is captured by a source Richardson number[19,46,47],

$$-\mathrm{Ri}_0 = \frac{-g'_0 r_0}{u_0}. \tag{2}$$

Here, $g'_0 = g(\rho_a - \rho_0)/\rho_a$ is the buoyancy of the jet mixture where $\rho_\mathrm{a}$ is the density of ambient water or atmosphere and $\rho_0$ is the bulk density of the mixture, $r_0$ is the jet radius and $u_0$ is the jet vertical speed, all taken at the source of the jet where it enters the ambient fluid. Usefully, $-\mathrm{Ri}_0$ can be defined for multiphase jets at their source in a water layer, in an air layer or at the water–air interface where submarine jets rise through a shallow water layer to enter an air layer. In general, where $-\mathrm{Ri}_0 > 10^{-4}$, jets rise in collapsing regimes to a maximum height $H_\mathrm{ftn}$ from which jet mixtures collapse periodically through the excitation of SWs[19,29,48].

Our deep-water and shallow-water analogues address the key control of eruptive source conditions expressed through $-\mathrm{Ri}_0$. In deep-water/subaerial regimes, without considering additional thermal buoyancy fluxes arising through the heating of entrained atmosphere[49] and water-vapour condensation[50], our predicted $H_\mathrm{ftn}$ in terms of the source conditions alone is a lower bound. However, the magnitude of our underestimate is unclear. The extent to which condensation enters quantitatively is equivocal[51]. Furthermore, whether these thermal effects supply a sufficiently large enough buoyancy flux to the mixture to cause an order of magnitude or more change in the mass flux partitioned between spreading ash clouds and PDCs, or drive the rise of gas and fine ash out of the mixture, at or before jets rise to $H_\mathrm{ftn}$ is also unclear.

For eruptions through shallow water layers with $D_\mathrm{SW} \leq 1$, our experiments are strictly analogous to sonic or subsonic (pressure-balanced) eruptions where turbulent instabilities cause entrainment and water ingestion to commence very close to the vent source[24]. Our experiments consequently overestimate water entrainment and underestimate natural fountain heights. Nevertheless, our reconstructed MERs for $D_\mathrm{sw} \ll 1$ in Fig. 5 are consistent with expectations on the basis of recent hydrovolcanic calculations by ref. 24, which conservatively limit water depths to be less than about 200 m for the inferred MER.

The particle volume fraction present in the jet mixture at the source is

$$\phi_0 = \frac{V_\mathrm{p}}{V_\mathrm{tot}}. \tag{3}$$

where $V_\mathrm{p}$ is the volume of particles in the mixture and $V_\mathrm{tot}$ is the total volume of the mixture. The particle volume fraction is used to calculate the bulk density of the mixture $\rho_0 = (1 - \phi_0)\rho_\mathrm{f} + \phi_0\rho_s$ where $\rho_\mathrm{f}$ is the interstitial fluid density at the source and $\rho_\mathrm{s}$ is the particle density.

In addition to particle volume fraction, particle size (inertia) and, to a lesser extent, density determine the particle–fluid coupling regime that affects the gathering and sedimentation of particles from explosive eruption columns, ash clouds and related PDCs[19,22,52–54]. Metrics for the particle–fluid coupling regime are the Stokes and sedimentation numbers:

$$\mathrm{St} = \frac{\tau_\mathrm{p}}{\tau_\mathrm{f}} \tag{4a}$$

$$\Sigma = \frac{\tau_\mathrm{f}}{\tau_\mathrm{s}}. \tag{4b}$$

Here, $\tau_\mathrm{p}$ is particle response time to fluid accelerations, $\tau_\mathrm{f}$ is the characteristic fluid flow timescale and $\tau_\mathrm{s}$ is the particle settling time. Where $\mathrm{St} \approx 1$ and $\Sigma \approx 1$, particle inertial and buoyancy effects modify the entrainment and sedimentation properties of eruption columns.

CCF eruptions occur in collapsing regimes where the excitation of SWs at the top of the momentum-driven fountain region of the eruption column is governed by well-established mechanics of turbulent fountains[19,29]. The rise height of a multiphase fountain can, consequently, be predicted on dimensional grounds with the spatially averaged source momentum and buoyancy fluxes:

$$H_\mathrm{ftn} = C M_0^{3/4} B_0^{-1/2}, \tag{5}$$

where $M_0 = \pi r_0^2 u_0^2$, $B = \pi r_0^2 u_0 g'_0$ and $C$ is determined with the source parameters[19,55–57]. Oscillations of the fountain about an average $H_\mathrm{ftn}$ occur at a frequency:

$$f_\mathrm{ftn} = C_\mathrm{ftn} B_0 M_0^{-1}, \tag{6}$$

where $C_\mathrm{ftn} \approx 0.5$ (refs. 19,29). Both $H_\mathrm{ftn}$ and $f_\mathrm{ftn}$ are defined at the source with subscript 0 and at the air–water interface with subscript i. Assuming particles are not lost from the fountain mixture during rise through the water column[47], the momentum and buoyancy fluxes of the fountain mixture entering the air layer can be estimated with measurements of the fountain radius and rise speed at the air–water interface.

The characteristic fountain frequency $f_\mathrm{ftn}$ is distinct from the buoyancy frequency $N$, which indicates the response of the stabilizing air or water-column density stratification to inertial effects of the fountain[19,29]. Where $f_\mathrm{ftn} > N$, the frequencies of sediment waves descending along fountain margins will be determined by both $f_\mathrm{ftn}$ and $N$, whereas where $f_\mathrm{ftn} < N$, the frequencies of these processes will be determined solely by the stratification, $N$ (ref. 19).

For deep-water fountains, depending on jet-source conditions (Fig. 5), the relatively low frequencies and high amplitudes of fountain-top height oscillations are governed by $f_\mathrm{ftn}$ and the frequency at which the ambient density stratification oscillates in response to the perturbation of the fountain,

$$N = \sqrt{-\frac{g}{\rho_{\mathrm{a},0}} \frac{\mathrm{d}\rho_\mathrm{a}(z)}{\mathrm{d}z}}, \tag{7}$$

where $\rho_{\mathrm{a},0}$ is the ambient density at the source height and the density stratification $\mathrm{d}\rho_\mathrm{a}(z)/\mathrm{d}z$ is assumed to be linear (Fig. 3a). We define $N_\mathrm{wtr}$ for water layers, $N_\mathrm{air}$ for air layers and $N$ for combined water and air layers.

For shallow-water fountains breaching the water surface, there are three additional modes that can contribute fountain-height oscillations: (1) $f_\mathrm{ftn}^\mathrm{air}$ defined for the subaerial part of the fountain; (2) the restoring stratification frequency $N$ of the combined water and air layers, defined with the density difference between the water layer and air over the maximum fountain rise height through both layers; and (3) $N_{\rm air}$ of the air layer defined using the density difference between the water layer and air over the subaerial fountain rise height (Fig. 3b). Low-frequency and high-amplitude fountain-height oscillations are governed by $N_{\rm wtr}$ and $N_{\rm air}$ whereas $f_{\rm ftn}^{\rm air}$ governs relatively higher-frequency and lower-amplitude oscillations. Fountain-top oscillations are an expression of the build-up and collapse of periodic SWs around the upflowing fountain core (Fig. 3a,b). An additional mode is corner frequency related to inertial effects of the breaking waves and overturning motions characterizing stirring as well as entrainment and mixing across density interfaces as SWs descend:

$$f_{\rm e}^{\rm sw} = \frac{u_{\rm sw}}{r_{\rm sw}}. \tag{8}$$

where $r_{\rm sw}$ and $u_{\rm sw}$ are the SW radius and speed as they descend next to the fountain. Usefully, we predict SWs to excite a distinctive and easily recognized fountain-top oscillation corresponding to this frequency (ref. 19).

Fountain mixtures collapsing periodically from $H_{\rm ftn}$ as SWs enter the water layer as momentum-driven jets with a characteristic jet entrance length scale[46]

$$l_{\rm sw} = Q_{\rm sw} M_{\rm sw}^{-1/2}, \tag{9}$$

where $Q_{\rm sw}$ and $M_{\rm sw}$ are the volume and momentum fluxes of sediment waves calculated with their measured $r_{\rm sw}$ and $u_{\rm sw}$ as they enter the water layer. This jet entrance length scale will govern, in part, whether SWs are erosive or depositional on impact with the ground.

The timing between SW impacts at the sea surface or seabed compared with the time for a SW to transform into a PDC and flow out of the SW impact zone will determine whether the spreading PDCs are fed intermittently or continuously. The ratio of an advective timescale for PDCs spreading out of the SW impact zone is $\tau_{\rm PDC} = r_{\rm im}/v_{\rm PDC}$ whereas the period between successive SWs is $\tau_{\rm ftn} = 1/f_{\rm ftn}$. The ratio of these two timescales forms the 'collapse frequency' number

$$\mathcal{F}_{\rm C} = \frac{\tau_{\rm PDC}}{\tau_{\rm ftn}}. \tag{10}$$

In the special limit $\mathcal{F}_{\rm C} \gg 1$, successive SWs coalesce such that periodic collapses typical of eruptions in collapsing regimes feed an approximately continuous mass flux to PDCs, resulting in massive or bedded deposits with negligible terracing. By contrast, as $\mathcal{F}_{\rm C} \rightarrow 0$, periodic column collapses drive increasingly discrete PDC events.

The MER of erupted material exiting the volcanic vent is a key source parameter used to compare eruption size and intensity and to initiate models of eruptions[25,36,58],

$$\mathrm{MER} = \rho_0 u_0 A_0, \tag{11}$$

where $A_0 = \pi[(r_0)^2 - (r_0 - \Delta r)^2]$ is the area of a ring vent geometry, with $\Delta r$ the vent width, and is associated with caldera-forming eruptions[22]. Constraints on MER after an eruption are typically inferred from observations of eruption column height and estimates of total mass erupted divided by eruption duration[58,59]. Column height and MER estimated in this way, however, do not explicitly constrain unique values of $-\mathrm{Ri}_0$ and $\phi_0$ and, in turn, are not ideal for predicting whether eruption columns will collapse periodically or continuously. To link values of $-\mathrm{Ri}_0$ and $\phi_0$ associated with realistic natural MER values in Fig. 5, we use a mean caldera fissure vent radius $r_0 = 4{,}000$ m and fissure width $\Delta r = 50$ m, mean particle density $\rho_{\rm s} = 1{,}500$ kg m$^{-3}$ and mean gas density $\rho_{\rm g} = 0.2$ kg m$^{-3}$ and vary the source velocity over $100 \le u_0 \le 330$ (refs. 21,35).

## Data availability

Source parameter data for experiments conducted in this study are presented in Table 1. Data for Figs. 2, 3 and 4 are available at https://doi.org/10.6084/m9.figshare.c.6432137.v1. Santorini bathymetry data are available at https://doi.org/10.7284/119607 and https://doi.org/10.7284/906516.

## Code availability

Code used for spectral analysis of fountain-top height oscillations and deposit profiles are available upon email request: jgilchri@eoas.ubc.ca.

## References

44. Gilchrist, J. T., Jellinek, A. M. & Hooft, E. Submarine terraced deposits linked to periodic collapse of caldera-forming eruption columns (Version 1). *Figshare* https://doi.org/10.6084/m9.figshare.c.6432137.v1 (2023).
45. Lherm, V. & Jellinek, A. Experimental constraints on the distinct effects of ash, lapilli, and larger pyroclasts on entrainment and mixing in volcanic plumes. *Bull. Volcanol.* **81**, 73 (2019).
46. Fischer, H. B., List, J. E., Koh, R. C. Y., Imberger, J. & Brooks, N. H. *Mixing in inland and coastal waters* (Academic Press, 1979).
47. Carazzo, G. & Jellinek, A. M. A new view of the dynamics, stability and longevity of volcanic clouds. *Earth Planet. Sci. Lett.* **325**, 39–51 (2012).
48. Hunt, G. & Burridge, H. Fountains in industry and nature. *Annu. Rev. Fluid Mech.* **47**, 195–220 (2015).
49. Woods, A. W. Turbulent plumes in nature. *Annu. Rev. Fluid Mech.* **42**, 391–412 (2010).
50. Glaze, L. S. & Baloga, S. M. Sensitivity of buoyant plume heights to ambient atmospheric conditions: implications for volcanic eruption columns. *J. Geophys. Res. Atmos.* **101**, 1529–1540 (1996).
51. Aubry, T. J. & Jellinek, A. M. New insights on entrainment and condensation in volcanic plumes: constraints from independent observations of explosive eruptions and implications for assessing their impacts. *Earth Planet. Sci. Lett.* **490**, 132–142 (2018).
52. Eaton, J. K. & Fessler, J. Preferential concentration of particles by turbulence. *Int. J. Multiph. Flow* **20**, 169–209 (1994).
53. Elghobashi, S. On predicting particle-laden turbulent flows. *Appl. Sci. Res.* **52**, 309–329 (1994).
54. Burgisser, A., Bergantz, G. W. & Breidenthal, R. E. Addressing complexity in laboratory experiments: the scaling of dilute multiphase flows in magmatic systems. *J. Volcanol. Geothermal Res.* **141**, 245–265 (2005).
55. Morton, B., Taylor, G. I. & Turner, J. S. Turbulent gravitational convection from maintained and instantaneous sources. *Proc. R. Soc. Lond. A* **234**, 1–23 (1956).
56. Bloomfield, L. J. & Kerr, R. C. Turbulent fountains in a stratified fluid. *J. Fluid Mech.* **358**, 335–356 (1998).
57. Bloomfield, L. J. & Kerr, R. C. Turbulent fountains in a confined stratified environment. *J. Fluid Mech.* **389**, 27–54 (1999).
58. Pyle, D. M. Sizes of volcanic eruptions. in *The Encyclopedia of Volcanoes* (eds Sigurdsson, H. et al.) 257–264 (Academic Press, 2015).
59. Mastin, L. G. et al. A multidisciplinary effort to assign realistic source parameters to models of volcanic ash-cloud transport and dispersion during eruptions. *J. Volcanol. Geothermal Res.* **186**, 10–21 (2009).

## Acknowledgements

This work benefited from thoughtful discussions with T. Druitt, O. Roche, B. Andrews, M. Manga, J. Dufek, E. Breard, C. Rowell, G. Valentine and R. Gallo. Sumisu bathymetry data were kindly provided by K. Tani. This project was funded through an NSERC

Discovery grant to A.M.J. E.E.E.H. was supported by NSF-OCE grant 2023338.

## Author contributions

J.G. and A.M.J. conceived the study and carried out the data analysis. J.G. designed and carried out the experiments with input from A.M.J. J.G. and A.M.J. wrote the paper with careful comments and input from E.E.E.H. S.W. helped with the experiments and produced digital elevation models of resulting deposits. E.E.E.H. produced the digital elevation model for Santorini using the Generic Mapping Tool and the profiles for both the Santorini and Sumisu deposits.

## Competing interests

The authors declare no competing interests.

## Additional information

**Supplementary information** The online version contains supplementary material available at https://doi.org/10.1038/s41561-023-01160-z.

**Correspondence and requests for materials** should be addressed to Johan T. Gilchrist, A. Mark Jellinek, Emilie E. E. Hooft or Sean Wanket.

**Peer review information** *Nature Geoscience* thanks Gert Lube, Arran Murch and the other, anonymous, reviewer(s) for their contribution to the peer review of this work. Primary Handling Editor: Stefan Lachowycz, in collaboration with the *Nature Geoscience* team.